THE JOURNAL OF PHYSICAL CHEMISTRY C

Article

Stability and Relaxation Mechanisms of Citric Acid Coated Magnetite Nanoparticles for Magnetic Hyperthermia

María Elisa de Sousa, Marcela Beatriz Fernandez van Raap, Patricia Claudia Rivas, Pedro Mendoza Zélis, Pablo Girardin, Gustavo A. Pasquevich, Jose L. Alessandrini, Diego Muraca, and Francisco H Sánchez

J. Phys. Chem. C, **Just Accepted Manuscript** • DOI: 10.1021/jp311556b • Publication Date (Web): 22 Feb 2013

Stability and Relaxation Mechanisms of Citric Acid Coated Magnetite Nanoparticles for Magnetic Hyperthermia

M. Elisa de Sousa[a] *, Marcela B. Fernández van Raap*[*a]*, Patricia C. Rivas*[a]*, Pedro Mendoza Zelis*[a]*, Pablo Girardin*[a]*, Gustavo Pasquevich*[a]*, Jose L. Alessandrini*[a] *, Diego Muraca*[b] *and Francisco H. Sánchez*[a]

[a] Instituto de Física de La Plata (IFLP- CONICET), Departamento de Física, Facultad de Ciencias Exactas, Universidad Nacional de La Plata (UNLP), c.c. 67, 1900 La Plata, Argentina. Tel +54 221 4246062 x 257 Fax +54 221 4236335

[b]Instituto de Física "Gleb Wataghin" (IFGW), Universidade Estadual de Campinas, Brazil

KEYWORDS

colloidal stability, magnetic fluid hyperthermia, relaxation mechanisms

ABSTRACT

Magnetite (Fe_3O_4) nanoparticles are proper materials for Magnetic Fluid Hyperthermia applications whenever these conjugate stability at physiological (neutral pH) medium and high specific dissipation power. Here, magnetite nanoparticles 9 - 12 nm size, electrostatically

stabilized by citric acid coating, with hydrodynamic sizes in the range 17 - 30 nm and well dispersed in aqueous solution were prepared using a chemical route. The influence of media acidity during the adsorption of citric acid (CA) on the suspensions long term stability was systematically investigated. The highest content of nanoparticles in a stable suspension at neutral pH is obtained for coating performed at pH = 4.58 corresponding to the larger amount of CA molecules adsorbed by one carboxylate link. Specific absorption rates (SAR) of various magnetite colloids, determined calorimetrically at a radio frequency field of 265 kHz and field amplitude of 40.1 kA/m are analyzed in terms of structural and magnetic colloid properties. Larger dipolar interactions, lead to larger Néel relaxation times, in some cases larger than Brown relaxation times, which in the present case enhanced magnetic radio frequency heating. The improvement of suspension stability results in a decrease of SAR values, and this decrease is even large in comparison with uncoated magnetite nanoparticles. This fact is related to interactions between particles.

TEXT

1. Introduction

Stable dispersion of magnetic nanoparticles (MNP) have attracted much attention, in a first stage because of their rheological properties[1] that allow a dynamic control by applied fields, and more recently due to their widespread biomedical diagnostic and therapeutic applications[2,3] such as visualization agents in magnetic resonance imaging[4], therapeutic carriers in drug delivery[5,6], heat intermediaries in cancer treatment therapies[7,8], and labelers for *in vitro* and *in vivo* separation experiments[9]. The usefulness of the magnetic colloids for biomedical application depends on their biocompatibility, the stability of the magnetic nanoparticles in solution at neutral pHs and the capability of MNP surfaces to become chemically functionalized.

Among many studied materials, Fe and its oxides are the unique FDA (US Food and Drug Admistration) accepted ones. The amphoteric surface of Fe oxides facilitates their funtionalization. Subsequently, many protocols have been developed for its preparation by either high-temperature decomposition of an organic iron precursor or low-temperature coprecipitation[10]. The MNPs produced by high-temperature decomposition methodology display better structural and magnetic properties but also hydrophobicity, then further work on MNPs surfaces for their stabilization in neutral conditions is needed. Stability in suspension is a major requirement for any biomedical application that involves injection in a living human being and results from the interplay between attractive dipolar and van der Waals interactions and repulsive electrostatic and steric interactions.

Steric stabilization includes coating with non-ionic surfactant molecules, polymers, and inorganic layers as silica or some noble metals[11]. Among the routes employed for obtaining the water soluble functionalized iron oxide MNPs, the addition of small biocompatible organic molecules, such as aminoacids[12], peptides[13], citric acid[14,15,16], and cyclodextrin[17] presents the advantages of combining electrostatic and steric stabilization, assuring coating biocompatibility and providing functionality for biomolecule conjugation. Polymeric stabilization comparing with electrostatic one presents the advantage of reversibility from the aggregated state by dilution, but usually involves the binding of a large macromolecule resulting in a coated MNP with a large overall size which strongly modifies its hydrodynamic behavior. So, a renewed interest has appeared in iron oxide nanoparticles synthesized by coprecipitation and stabilized by functionalization of their surface using small molecules with large deprotonation ability like organic polyprotic acids, leading to electrosteric stabilization.

Citric acid (AH_3 with A= $C_6H_5O_7$) is a small molecule that has three carboxyl and one hydroxyl groups and is known to chemisorb to iron oxide nanoparticle by forming a carboxylate group

with the Fe-OH molecules present on the nanoparticle surface, leaving one or two carboxyl groups negatively charge that can be used for other purposes. A positively charged drug[16] and/or a fluorescent molecule, like for instance rhodamine[18], can be bonded to them for applications in drug delivery or for *in-vitro* labeling studies, respectively. As the AH_3 molecule is small the nanoparticles hydrodynamic radii are not much enlarged, which is of importance in magnetic hyperthermia therapy applications. Differences evidenced in the rheological and microstructural properties of biocompatible citric acid coated magnetites prepared by different protocols based on the coprecipitation method have been recently discussed elsewhere[15].

Magnetic Fluid Hyperthermia is a therapy to treat cancer tumors. Briefly, MNPs exposed to a radio frequency (*rf*) field, absorbs energy from the applied field and dissipate this energy through magnetic relaxation effects locally raising the tumor temperature above 43 ºC and selectively killing tumor cells[7]. The figure of merit of a given nanoparticle for this application is given by the specific absorption rate (SAR), which is defined as the heat power absorbed from the *rf* field per gram of magnetic material. Nowadays, active research is being executed on MNPs synthesis protocol to improve specific absorption rates in order to reduce the amount of material that has to be incorporated into a given tumor for its treatment and also in order to extend this kind of therapy to smaller tumors, which requires the attainment of larger SAR values. For single-domain MNPs, relaxation processes are of the Néel and Brown types. These processes correspond to the nanoparticle magnetic moment switching among its easy axis directions and the viscous friction due to the Brownian rotational diffusion of particle in the fluid, respectively. As both processes take place in parallel, the heating is driven by the one having the shorter characteristic time[19]. From the stabilization ways previously outlined, emerges either the possibility of using MNP with large hydrodynamic sizes (polymeric like coating) possibly resulting in Néel driven process or using MNP covered with small organic molecules, as the ones

studied here, which may dissipate through a Brown type process. The question of which of these mechanisms optimizes the heating process is still an open question, whose answering requires more experimental research.

In this work, highly stable and biocompatible magnetic suspensions of citric-acid coated Fe_3O_4 nanoparticles in water were produced as biomedical colloids suitable for energy dissipation under an external ac magnetic field in the *rf* range and appropriated for magnetic hyperthermia therapy. Moreover, the specific heating efficiency at a frequency of 265 kHz and field amplitudes of 20, 27.8 and 40.1 kA/m were determined and are discussed here in terms of the MNPs structural and magnetic parameters. Optimum synthesis conditions for long term suspension stability, as well as the performance of the obtained ferrofluids for *rf* heating, are determined for a wide range of experimental conditions. A detailed analysis of SAR measured values in terms of magnetic and structural colloid properties is addressed. Finally, the coated MNP were efficiently internalized by human lung adenocarcinoma A549 cells and its viability was analyzed by flow cytometry using Annexin V - Propidium Iodide (PI) markers.

2. Experimental details

Fe_3O_4 nanoparticles (core) were prepared by co-precipitation of ferric chloride and ferrous chloride in the presence of excess ammonia NH_4OH solution (AS) via a modified Massart method[20,21]. The so obtained magnetite cores were negatively charged by CA adsorption over its surfaces. The coating was performed without leaving the wet route, in order to avoid nanoparticle surface passivation. Both steps, co-precipitation and CA adsorption, were carried out under a N_2 reflux, to assure anaerobic conditions, with continuous and vigorous magnetic stirring to assure reagents homogeneity, and at controlled constant temperature equal to 60 °C. The heating device was close loop controlled in order to assure temperature homogeneity and reproducibility.

Briefly, 2.75g of $FeCl_3.4H_2O$ and 1.01g of $FeCl_2.6H_2O$ were dissolved in 50 ml of bidestilled water each, mixed in a three-neck flask, and heated to the reaction temperature. Then, 3 ml of AS (25 % w/w) was added drop by drop and left to react for 30 min, after that, 75 ml of AS were added at a rate of 1 drop/s until the solution reach a pH of 10.5, high enough to prevent agglomeration due to surface charge. Isoelectric point (IEP) of magnetite is known[22] to be in the pH range from 6 to 7 depending on the Fe^{2+} concentration and temperature. Then, the black precipitate was separated from the dispersion medium by means of a permanent magnet, mixed with a CA aqueous solution (0.02 g/ml), and left to react at 60 °C during 90 min to obtain citric acid coated magnetite. To yield uncoated magnetite (*u*), the black precipitated was washed several times and resuspended in water at a pH close to neutral one (7- 7.4).

The pH at which CA was adsorbed to the MNP surface (pH_{ad}) was varied from 4.58 to 7.08. AS (0.25 % w/w) was used to adjust the suspension pH to pH_{sus} close to 7. Then the suspension was again placed in a permanent magnet during 600 s. By this way six colloids C_i (with i=1 to 6 for increasing pH_{ad}) were prepared. Each one of them was then divided in two parts: the suspension of MNPs that were immobilized with a permanent magnet (CP_i) and the suspension of the MNPs which remained suspended under the moderate magnetic field created by the magnet (CS_i). Details about the preparation of the six CS_i colloids of Fe_3O_4 nanoparticles coated at different pH_{ad} are given in table I. pH measurements were carried out with a pH-meter with ±0.01 pH accuracy.

Common and standardized chemical volumetric analysis was used for colloid concentration [x] determination, expressed as magnetite mass per solvent volume with an accuracy of 2 %. $K_2Cr_2O_7$ was used as titrant.

Phase identification and core particle characterization were performed by X-ray diffraction (XRD) and Transmission Electron Microscopy (TEM) on dried samples. Dried coating easily

hydrates hindering sample preparation for XRD analysis, especially in the more efficiently coated cases. The patterns were determined with a X'Pert Diffractometer within a 2θ range from 20 to 80 degrees. TEM images were obtained with a TEM JEOL JEM 2100 microscope.

Zeta-potential measurements and Thermogravimetry (TG) combined with differential thermal analysis (DTA) were used to confirm coating achievement. Measurements were carried out on dried powder samples with a Shimatzu TG-50 and DTA-50 system. During measurements the samples were kept inside platinum crucibles and heated at a constant rate of 10 K/min under a flux of 50 ml/min of N_2. Laser Doppler Electrophoretic method was used to measure zeta-potentials (ζ [mV]) of 1 ml of colloid with a Malvern Zetasizer nano ZS90 device. The zeta potential was obtained by the application of Henry equation using Hückel approximation.

Dynamic light scattering (DLS) experiments were performed on CS_i colloids at scattering angle 90°C with a goniometer ALV/CGS-5022F with Multiple Tau digital correlator ALV-5000/EPP.The light source was an helium-neon laser operating at 22nW.

Specific magnetization (M) as a function of applied magnetic field (H) at room temperature was obtained using a VSM LakeShore 7404 vibrating sample magnetometer operated with a maximum applied field $\mu_0 H_{max}$= 1.5 Tesla or with a SQUID Quantum Design magnetometer with $\mu_0 H_{max}$ = 2.5 Tesla. The later was also used to measure the magnetization temperature dependence under zero field cooled (ZFC) and field cooled (FC) protocols carried out at 2 K/min and H_{FC}=100 Oe.

Hydrodynamic sizes were obtained from the inverse Laplace transformation of the measured time correlation function assuming the Stokes-Einstein relation between relaxation times and hydrodynamic diameters[23]. Each sample was measured 10 times. Mean values (d_H) of the weight-average hydrodynamic sizes are reported in Table I.

Time-dependent calorimetric experiments were conducted exposing 1 cm^3 of the colloid, hold in a clear glass Dewar, to *rf* fields of 20, 27.8 and 40.1 kA/m amplitude and 265 kHz frequency. The temperature was sensed during treatment with a fiber optic sensor placed at the center of the sample. The sensor was connected to a calibrated signal conditioner (Neoptix) with an accuracy of ± 0.1 C. Colloid temperature was kept below 65 °C in order to minimize evaporation and prevent colloid destabilization.

SAR parameter was obtained from the initial slope of the heating curve with the expression

$$SAR = \frac{C}{[X]}\frac{\partial T}{\partial t} \qquad [1]$$

where C is the volumetric heat capacity of the solvent (C=4.18 J/ K cm^3), and [x] the MNP concentration given as mass of Fe_3O_4 per solvent volume unit.

Viability and discrimination of apoptotic and necrotic cells was determined by double-labeling for Annexin V and PI assay, and analyzed by flow cytometry using a PARTEC PAS III cytometer. It is known[24] that the plasmatic membrane loss phospholipid asymmetry in the apoptosis, resulting in the exposure of phosphatidylserine (PS) residues at the outer plasma membrane leaflet. Annexin V interacts strongly and specifically with PS and it is used to detect apoptosis by targeting for this asymmetry. Annexin V does not bind to normal live cells since the molecule is not able to penetrate the phospholipid bilayer. In necrotic cells the integrity of the plasma membrane is lost then Annexin V is able to bind to cell. To discriminate between necrotic and apoptotic cells PI (a membrane impermeable DNA stain) is simultaneouly used.

A549 cells were grown as monolayer in Dulbecco's modified Eagle's medium (DMEM) supplemented with 10 vol.% fetal bovine serum, and 0.5 mg ml^{-1} streptomycin in a humidified 5% CO_2 atmosphere at 37 ^oC. For the MNP uptake, the cultures at 60 % confluence (24 h incubation time) were washed with phosphate buffered saline (PBS) and were incubated, in 18

ml DMEM doped with three distinct concentrations of 34, 67, and 135 μg_{Fe3O4} /ml culture medium, in 75 cm^2 flask during 12 h. Then, cells were washed four times with PBS to remove the non incorporated MNPs and trypsinized from each flask. From each A549 internalized culture10^6 cells were resuspended in Annexin-binding buffer and stained with 5 µl of Annexin and 5 µl of propidium iodide. Cells incubated without nanoparticles at the same condition of the internalized ones (36 h incubation time) were used as control.

3. Results and discussions

3.1 Stability analysis

The crucial step in the preparation of a stable aqueous suspension of MNPs resides on their surfaces engineering, in this case on the CA adsorption efficiency. Representative DTA-TG curves of citric acid and CS_i colloid are shown in figure 1a and 1b respectively. DTA curve at figure 1 a) displays a sharp endothermic peak at 157 °C without weight loss at the corresponding TG, assigned to fusion (ΔH_{fus}=-0.14 kJ/g) and a broad endothermic feature (centered at 217 °C) assigned to citric acid decomposition (ΔH=-0.55 kJ/g), happening in many steps. TG data shows an abrupt single step weight loss (onset at 209 °C) of 87.5 % due to AC decomposition. On the other hand, no fusion peak appears at DTA curve (figure 1b) of coated nanoparticle indicating the absence of free CA precipitation, exothermic peaks related to magnetite oxidation commencing around 200 °C are superimposed to attached CA decomposition. TG curve displays a two step weight loss (onsets at 175 and 222 °C) of 7.3 and 2.5 % which are attributed to desorption of citric acid molecules from the nanoparticle surface[18]. Two step weight loss is an indication of a bilayer coating formation, at the first layer the CA molecules are chemically attach to MNP surface and the second is bind to the first through hydrogen bonds. The later desorbs at lower

temperature. Two step weight loss has been observed at MNP coated by bilayers of n-alkanoic acids[25]. From the comparison of these thermogravimetric curves it is inferred that the binding of CA molecule to MNP surface was accomplished.

Both types of aqueous suspensions (CP_i and CS_i) are very stable and the MNPs remain suspended for periods of several months, being CS_i colloids extremely stable. For CS_i colloids the separation of the MNPs from the dispersion media was not even possible by three times centrifugation at 13000 rpm during 600 s. The mass fraction (f) of suspended nanoparticles, defined as the quotient of concentrations, measured at pH_{sus}, $f = [CS_i]/[C_i]$, was used as a parameter to quantify the CA adsorption efficiency and as a long term stability criterion. In figure 2, it can be seen that f decreases monotonically with pH_{ads}. The aqueous citric acid solution left to react with the oxide particles during the synthesis consists of a pH dependent mixture of AH_3, AH_2^-, AH^{2-} and A^{3-}. The molar fractions x_y (y = AH_3, AH_2^-, AH^{2-} and A^{3-}) calculated using the known acid dissociation constant pKa_1=3.13, pKa_2=4.76 and pKa_3 = 6.40 are included in figure 2. The larger f value is achieved for CA adsorption at pH_{ads}= 4.58, when 60 % of CA molecules were negatively charged as AH_2^- and 40 % as AH^{2-}. The decrease of AH_2^- and AH^{2-} occurring at pH larger than 5.5 disfavors stability. At pH values lower than 4.58 there is a large dissolution rate and the MNP dissolves during preparation[26].

Zeta-potentials (ζ) measurements of CS_2, CS_4, CS_6 and u colloids are shown in figure 3 and the mean ζ values against pH are displayed in figure 4. The isoelectric point (IEP) of coated nanoparticles is close to 2 and for pH > 4 the largest mean value of ζ is close to -36 mV. Results suggest that at larger pH_{sus} stability occurs when larger amount of AH_2^- is present at binding condition, i.e. larger amount of CA binds to the nanoparticles surfaces by one carboxylate leaving two free dangling ends. Further deprotonation of already bonded molecule

occurs at pH value larger than pKa_3 = 6.40, providing electrostatic and steric stabilization. Mean ζ values as large as -36 mV confirms that the particles have become high negatively charged, and that the coating was accomplished. Our results differ from a previous work[14] where the largest amount of magnetic nanoparticles in stable suspension at pH_{susp}= 10.1 was obtained with CA adsorption at 80 °C and pH_{ads}=5.2 where 70 % the molecules are twice deprotonated as AH^{2-} and 25 % once deprotonated, however the largest $|\zeta|$ determined in both works coincide because both were measured at pH values larger than pKa_3 where the three carboxyl groups are dissociated. A largest ζ value of -25.6 at pH 6 was obtained in other recent work[16] were coated magnetite was optimized for drug delivery. A lower ζ value means less charge and may be related to a shorter adsorption time (30 min less).

3.2 Structural and Magnetic Analysis

X-ray diffractograms for *u* and CS_i samples present typical x-ray diffraction patterns of magnetite (See Figure at Supplementary Information). The diffraction patterns display well defined peaks belonging to the cubic spinel structure, indicating that the samples are single phase. The whole patterns were refined, including peak broadening due to crystallite size, using a cubic spinel structure (space group Fd3m) with lattice parameter a = 8.378 Å and the O atoms arranged in a face centered- cubic lattice. Figure 5a displays a typical TEM image of *u*-MNPs (d_{TEM} = 9.9 ± 2.4 nm). These particles are not regularly facetted, instead they show spheroid-like forms and are quite aggregated. A representative TEM image of a coated colloid (CS_6) is shown figure 5b and a single CS_6 particle in figure 5c. Selected area electron diffraction pattern indicates good crystallinity (see inset of figure 5c). The MNPs are spherical, more uniform and further

apart from each other than uncoated nanoparticles. Chain like arrangements due to dipolar interactions appear. Mean size values estimated from TEM data are listed in table I. CS_i and CP_i colloids display similar mean size, for example d_{TEM} for CP_6 is 10.8 ± 2.7 nm.

Magnetic analysis was performed on dried colloid samples and on frozen uncoated and both CS_i and CP_i coated colloids. Each sample is a collection of single domain particles of magnetic volume V, and giant magnetic moment $\mu=M_s\rho V$ (ρ the mass density). Particles magnetocrystalline anisotropy axes are randomly distributed. The energy of this ensemble placed in a magnetic field H arises from three main contributions, the magnetic anisotropy energy, the particle magnetic moment Zeeman interaction with the applied field, and the dipolar interaction among particles.

The first and third energy terms dominate at low field, and then determine the magnetization behaviour as a function of temperature in FC and ZFC curves displayed in figure 6 for u and CS_2 samples. The absence of a maximum in the ZFC curve of the u sample indicates a blocking temperature room temperature due to aggregation and strong dipolar interaction between particles. The constancy of M almost in the whole FC curve is also a signature of a highly interacting system. The ZFC curve of CS_2 exhibits a maximum at the blocking temperature T_{Bi} = 92 K, and ZFC bifurcates from FC curve at the irreversibility temperature Ti = 140 K. For temperatures higher than Ti magnetization temperature dependence strongly departs from the Curie-like behavior ($M \sim H / T$) expected for a non interacting system. As temperature decreases from Ti the FC magnetization increases. Comparing ZFC-FC curves of uncoated and coated MNPs it is clear that citric acid coating prevents strong aggregation and lowers dipolar interaction, but still the system behaves as an interacting superparamagnet (ISP). Colloids blocking temperatures T_{Bi} obtained from ZFC data acquired from frozen colloids are listed in table I.

The second energy term dominates at high fields and is the main contribution to the hysteresis loops shown in figure 7. The mean particle magnetic moment $<\mu>$ in all the studied samples is around 1.5 x 10^4 μ_B, the anisotropy energy barrier $K_{eff}V$ is much smaller than the magnetic moment field interaction energy $\mu_0\mu H$ and the magnetization of the particles at a given temperature and field can be modeled as:

$$M(T,H) = N\int_0^\infty \mu L\left(\frac{\mu_0\mu H}{k_B T}\right) f(\mu)\, d\mu + \chi_a H \qquad (2)$$

where the Langevin function $L(x) = \coth(x) - 1/x$, being $x = \mu_0\mu H / kT$, is convoluted with a log-normal distribution of magnetic moments $f(\mu) = \exp\left[-(\ln(\mu/\mu_m)/2\sigma^2)\right]/\mu\sigma\sqrt{2\pi}$ and χ_a is the high field susceptibility[27] related to surface magnetic disorder induced by the lack symmetry. Not fully coordinated atoms at the surface of the particle lead to a magnetically frustrated layer which does not saturate even at 10 K and 2000 kA/m (see inset at figure 7). The specific saturation magnetization is $M_s = N\langle\mu\rangle = N\int_0^\infty \mu f(\mu)\, d\mu$, where N is the particle number mass density and $<\mu>$ the mean magnetic moment. χ_a values are of the order of 10^{-7} m^3/Kg. Although the cycles are well fitted with eq. (2), and the derived M_s values are correct, the so obtained mean magnetic moments display an unexpected temperature dependence[28]. In figure 8 the mean values $\langle\mu\rangle = \mu_m \exp(\sigma^2/2)$ for various CS_i samples, obtained from best fits of M vs. H data of dried colloid powders and frozen colloids, display an increasing behavior with temperature which is characteristic of ISP systems. Then, in order to determine the particle size distribution from the magnetic properties of each colloid and to compare it with the results obtained by TEM, $<\mu>$ is derived from M vs. H data acquired from colloidal samples at room temperature (see figure 7) where the effect of the dipolar interaction on the recorded pattern is

diminished. Using $\mu = M_s^{bulk} \rho V$ with magnetite density ρ=5175 kg/m^3 and M_s^{Bulk}= 86 Am^2/kg, a lognorm number distribution of magnetic core diameters $f(d_m)$ (with median $d_0 = \left(6\,\mu_0 / \pi\, M_s^{bulk} \rho\right)^{1/3}$ and $\sigma_{d_m} = \sigma / 3$ for spherical particles) is derived from $f(\mu)$ (see figure 9). From mean $<d_m>$, mean nanoparticle size is derived as $d =< d_m > + \delta$ with $\delta =< d_m > \left((M_s^{bulk} / M_s)^{1/3} - 1\right)$ twice the magnetically frustrated surface layer thickness. From this analysis, it is concluded that the colloids CS_i and CP_i under study here, are single domain and behave as interacting superparamagnets. For CS_1, CS_2 and CS_6 samples the size derived from magnetic cycles are larger than the mean sizes derived by TEM while for CS_3, CS_4 and CS_5 the agreement is good. This discrepancy can be ascribed to the fact that TEM, although being a more direct determination, involves a smaller number of particles than the macroscopic magnetic measurement.

A charged particle moving in a solvent drags with it a layer of fluid molecules and counter ions, resulting in an entity with a quite large hydrodynamic diameter d_H. In effect, in this study it was found that d_H values are one order of magnitude larger than the overall nanoparticle size including CA coating (see table I).

3.3 Specific absorption rates (SAR)

The heating ability of the various colloids analyzed here was calorimetrically determined and typical heating curves are shown in figure 10. The time required to reach a given temperature, at fixed frequency, decreases with increasing field amplitude. SAR represents the power released per gram of magnetite upon ac-field application and is mainly given by the magnetization loop area. SAR values listed at table I and II were obtained from the initial slope of the heating curves using formula (1). These values range from 5.2 to 41.5 W/g for CS_i colloids, from 29 to 104 W/g

for CP_i, and 203 W/g for *u*-MNP colloid. The inspection of figure 9 shows that for our samples there is no clear relation between SAR values neither with magnetic core sizes nor with distribution standard deviation σ_{dm}. For instance, CS_6, CS_4 and *u* colloid dissipates 5.2, 41.5 and 203 W/g respectively and all have nearly the same mean size. Main differences between these samples reside on saturation magnetization and blocking temperatures. Lower saturation magnetizations are assigned to larger magnetically frustrated layers, and larger blocking temperatures to interaction and aggregation.

Now we evaluate SAR data in terms of the colloids physical characterization given by *Ms*, $<d_m>$, δ, T_{Bi} and d_H parameters listed in table I and II.

Through the linear response theory SAR parameter is theoretically given by[19]

$$SAR = \frac{\pi \mu_0 H_0^2 f}{\rho} \int_0^\infty \chi''(\tau(d)) f(d)\, dd \qquad (3)$$

where μ_o is the permeability of free space (4π x 10^{-7} H/m), *f(d)* is the size distribution of MNPs having diameters *d*, and χ'' is the out-of-phase magnetic susceptibility. SAR field amplitude dependence, plotted in figure 11, displays an increasing behavior as expected from formula (3). The dependence departs from the linear relation expected for SAR plotted against H_0^2 for H_0 values larger than a maximum field. Once this field is exceeded the area of the hysteresis loop does not change and SAR remains constant.

For non interacting nanoparticles χ'' is a function of the relaxation time (τ) as

$\chi''(\omega) = \chi_0 \frac{\omega\tau}{1+(\omega\tau)^2}$; with $\omega = 2\pi f$ and the dc-susceptibility $\chi_0 \cong \frac{\mu_0 \rho^2 M_s^2 V}{3k_B T}$, for small magnetic field amplitude. Because the colloids behave as interacting superparamagnets the dynamics of such systems strongly depends on many physical parameters related with the MNP

properties and on the coupling strength. Weather the relaxation is driven by Brown ($\tau_B = \frac{3\eta V_H}{k_B T}$) or by Néel ($\tau_N$) mechanisms depends on liquid carrier viscosity η, hydrodynamic particle volume (V_H), magnetic energy barrier E_a and attempt time τ_0, being both E_a and τ_0 size dependent[29]. The processes take place in parallel ($\tau^{-1}=\tau_B^{-1}+\tau_N^{-1}$) and prevails the one having the shorter relaxation time.

τ_B values calculated at 300 K using data listed in table I and η = 8.90 10^{-4} Pa s for water, fall in the range 0.2 x10^{-5} - 0.9 x 10^{-5} s and are plotted vs. SAR at figure 12.

τ_N for isolating particles is given by[30] by $\tau_N = \tau_0 \exp(\sigma)$ with $\sigma_a = E_a/k_B T$ (4)

The energy E_a of isolated particles is equal to the magnetic anisotropy energy $K_{eff}V$ and K_{eff} is the size dependent effective anisotropy energy density. For spherical particles, assuming that the overall anisotropy of the particle is uniaxial, the relation $K_{eff}(d)=K_{bulk}+(6/d)K_s$ is commonly used, where K_{bulk} = 1x10^4 J/m^3 is the bulk anisotropy energy density of magnetite at room temperature and K_s is the surface anisotropy density. This $K_{eff}(d)$ relation models the increase of the anisotropy energy density with decreasing particle size and has been tested by K. Gilmore et al.[31] in magnetite particles grown inside three protein cages of distinct size, where the cage served to constrain particle size and shape and to mute interparticle interaction. Using this relation with $K_s(d)=2$ tanh$(d/4)$, as in ref 31, we have retrieved K_{eff} for each particle size listed in table I. The corresponding τ_0 values were interpolated from $\tau_0(d)$ relation built from data in references 31 and 32. Evaluation of τ_N disregarding interactions results in values in the range 0.1 – 0.6 x 10^{-9} s.

To take into account that the magnetic moments of interacting particles fluctuate with different relaxation times than those of isolated ones, a total energy barrier given by $E_a = K_{eff}V+E_{int}$ was assumed[33]. The interaction energy E_{int} was deduced from the shift of ZFC maximum (figure 6),

disregarding τ_0 dependence with interactions, with respect to a non interacting ensemble as $E_{int} = k_B(T_{Bint}-T_B)ln(t_m/\tau_0)$. Here T_B is the blocking temperature expected for non interacting particles of sizes listed in table I, as derived from the K_{eff} and τ_0 values mentioned above, T_{Bint} is the blocking temperature resulting from ZFC measurements (see table I), and t_m~100 s the SQUID measuring time. Then, Néel relaxation time for interacting particles τ_{Nint} was obtained with formula 4 with $\sigma = (K_{eff}V + E_{int})$. The results are shown in figure 12 where the relaxation times are plotted vs. SAR values determined with H_0=40.1 kA/m i.e maximum used H_o value, larger than the anisotropy field. Interaction results in slower magnetic relaxation. A crossover between τ_{Nint} and τ_B behavior appears at 12.8 W/g. The larger SAR values come out with the more interacting colloids i.e for the particles displaying larger T_{Bi} (large E_{int} values). In those cases the process seems to be driven by Brown mechanism while for the other cases Néel mechanism prevails.

The uncoated magnetite results in a very unstable suspension but produces the largest SAR of 200 W/g. Although particle size is alike to those of coated particles the hydrodynamic size is 1.5 μm (polydispersity index σ_{PI}=0.5) indicating the presence of large clusters of particles moving in the fluid. Blocking temperature is around 300 K, due to strong interactions. The analysis outlined above for coated colloids, when applied to the uncoated colloid results in relaxation times various orders of magnitude larger. Still $\tau_B < \tau_{Nint}$, supporting the idea that interactions play an important role in magnetic fluid hyperthermia increasing nanoparticles energy dissipation.

SAR values against M_s are plotted in figure 13 for all CP_i, CS_i and u colloids. An increasing behavior is observed, as expected from χ_0 dependence with M_s irrespectively of nanoparticle size and dispersion. Lowering of M_s is assigned to a larger magnetically frustrated layer. Those CS_i colloids of MNP coated at lower pH_{ads} and displaying larger electrostatic stability present lower M_s values. The corresponding CP_i colloids display larger M_s and SAR values consistently with

the idea of MNPs having less coating material on their surfaces and being more effectively attracted to the magnet. These observations suggest that citric acid may have an influence on the surface of the MNP, producing larger frustrated layers which on one side improve nanoparticle suspension stability but on the other one lower SAR values. The optimum synthesis condition in order to accomplish both properties, extremely high stability in suspension at neutral *pH* and large SAR values is obtained by citric acid coating at pH_{ads}=6.25.

3.4 In vitro biocompatibility of CA-coated MNP internalized in A549 cells

The materials involve in the synthesis procedure (water, CA and magnetite) are known to display good biocompatibility. However, since interfacial processes may take place when MNPs are dispersed in biological media changing their surface reactivity and consequently their toxicity[34] we have tested the viability of our nanoparticles in A549 cells. Figure 14 shows the cytometric analysis of double-labeling for Annexin V and PI assay for A549 cell without MNPs exposure and internalized with three distinct CS_4 colloid concentrations. Viable cells are negative for both labelers (DL quadrant), apoptotic cells are PI negative and annexinV positive (DR quadrant), while necrotic cells are positive for both (UR quadrant). After internalization with CS_4 colloids at concentrations of 34, 67, and 135 μg_{Fe3O4}/ml, the percentages of viable cells are 94.7%, 95.1%, and 81.3%, respectively. Only for the highest concentration viability decrease compared with 84.7% of control cells is observed. The fact that the control culture shows a lower viability than the lower concentrated cultures may be due to an overgrown control culture. It is concluded that 12 h exposure to CA coated Fe_3O_4 nanoparticles at low concentration is not altering A549 cell viability. Then, citric acid coated magnetite aqueous suspensions at neutral *pH* were internalized without causing cell toxicity.

Conclusions

We have presented a detailed and extensive study of synthesis conditions, magnetic properties, and radiofrequency dissipation efficiency of various biocompatible citric acid coated magnetite aqueous suspensions at neutral *pH*. Preparation method enables to control the long term stability of the suspension varying the citric acid adsorption *pH*. Largest stability at neutral medium is achieved for the nanoparticles coated at *pH* of 4.58, where citric acid mainly binds to the particle surface by one carboxylate leaving two free and charged dangling ends. Citric acid influence the surface of the MNP, producing thick magnetically frustrated layers which on one side improve nanoparticle suspension stability but on the other one reduce SAR values. Finally, our results indicate that dipolar interactions between the nanoparticles play a key role in Néel relaxation mechanism and dissipation efficiency. Magnetic relaxation becomes slower for interacting colloids and heating efficiency increases. Largest SAR values arise from the more interacting nanoparticles, a case where Néel relaxation times become larger than Brown relaxation times leading to Brown dissipation mechanism to prevail. It is shown that SAR data cannot be easily reproduced using the magnetic data and the most currently used theoretical expressions, due to the presence of dipolar interactions between the nanoparticles. Interaccion energy was included in the theoretical expressions through the quantity $\sigma = \left(K_{eff}V + E_{\text{int}}\right)/k_BT$ and its value inferred from the blocking temperature shift.

FIGURES

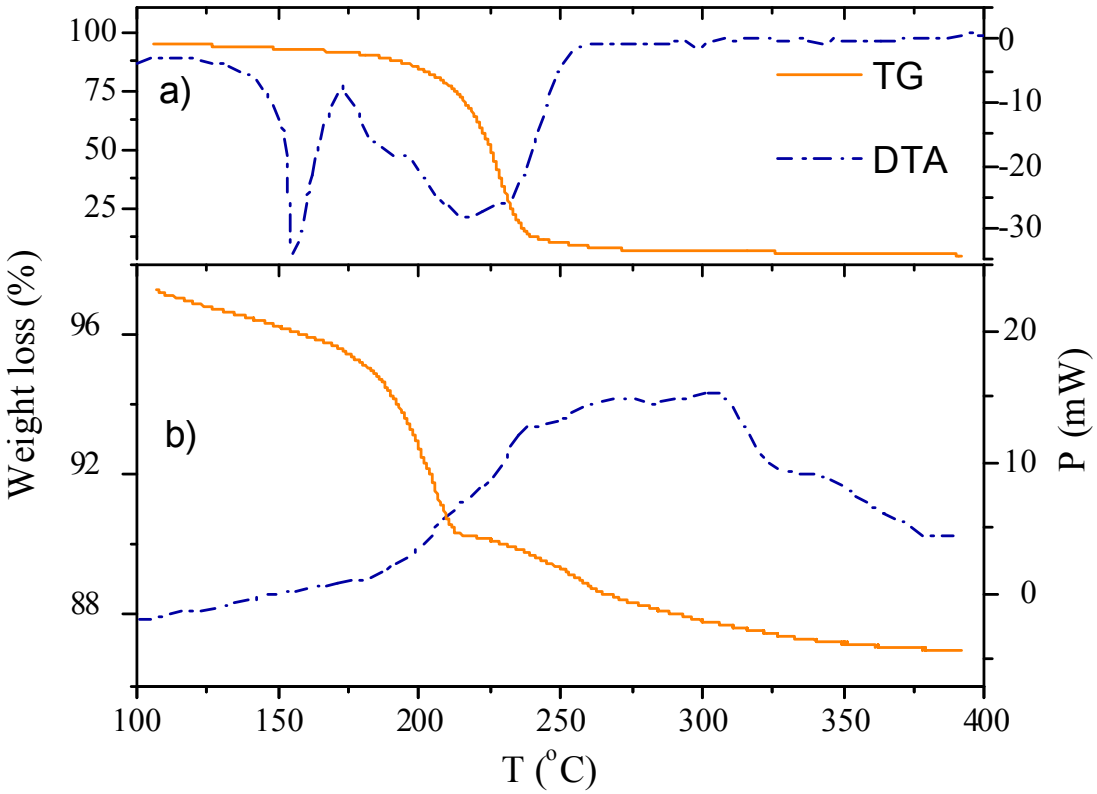

Figure 1: TG and DTA plots of neat citric acid at upper part (a) and CS_i colloid at lower part (b).

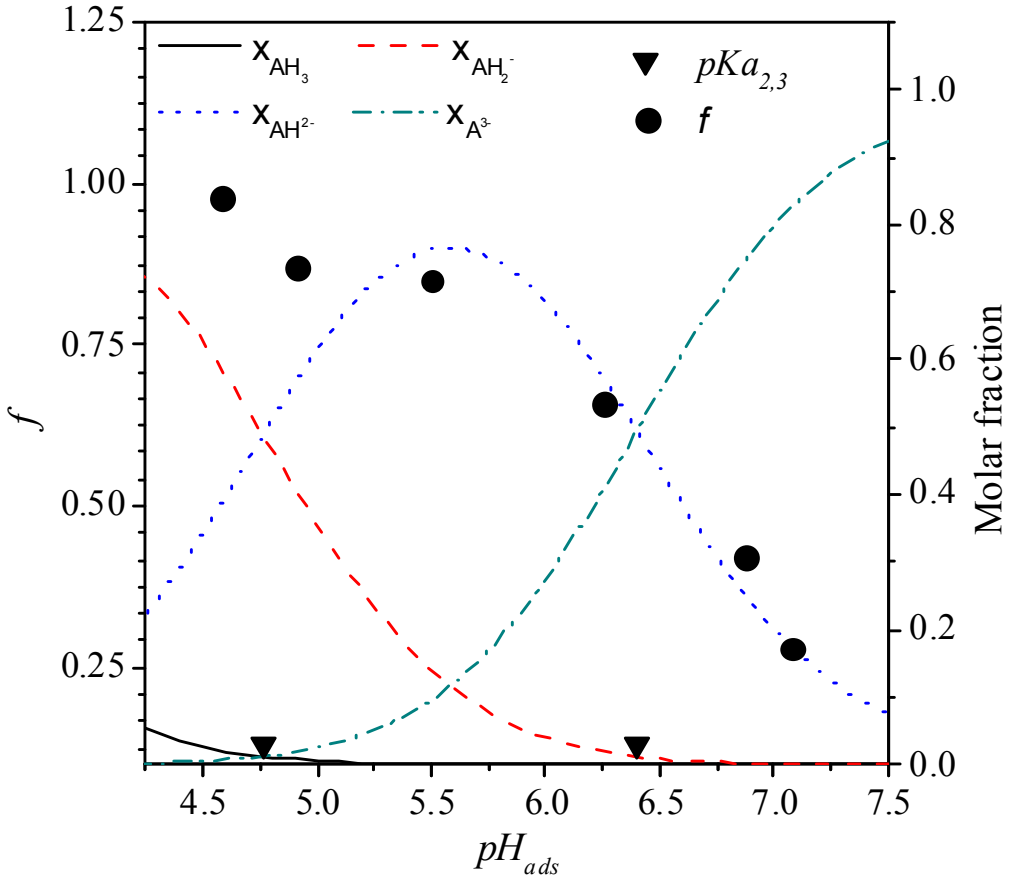

Figure 2: Dots stand for the fraction (*f*) of MNP that remains stable at neutral pH after exposure to 0.1 T during 600 s, used as long term stability parameter, triangles for acid dissociation constants (*pKa*) and pH_{ads} for adsorption pH. Lines stand for theoretical calculations of molar fraction of the species composing the aqueous citric acid solution vs. adsorption pH_{ads} using equilibrium dissociation constants for deprotonation reactions.

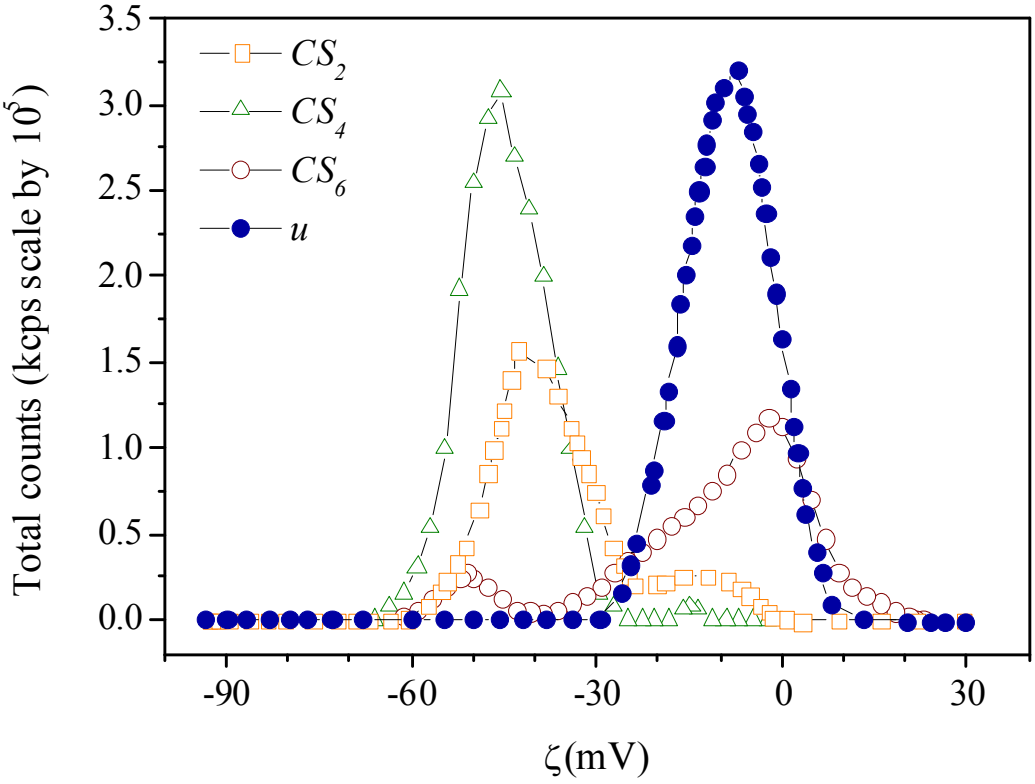

Figure 3: Zeta potential (ζ) distribution of coated MNP measured at neutral suspension pH.

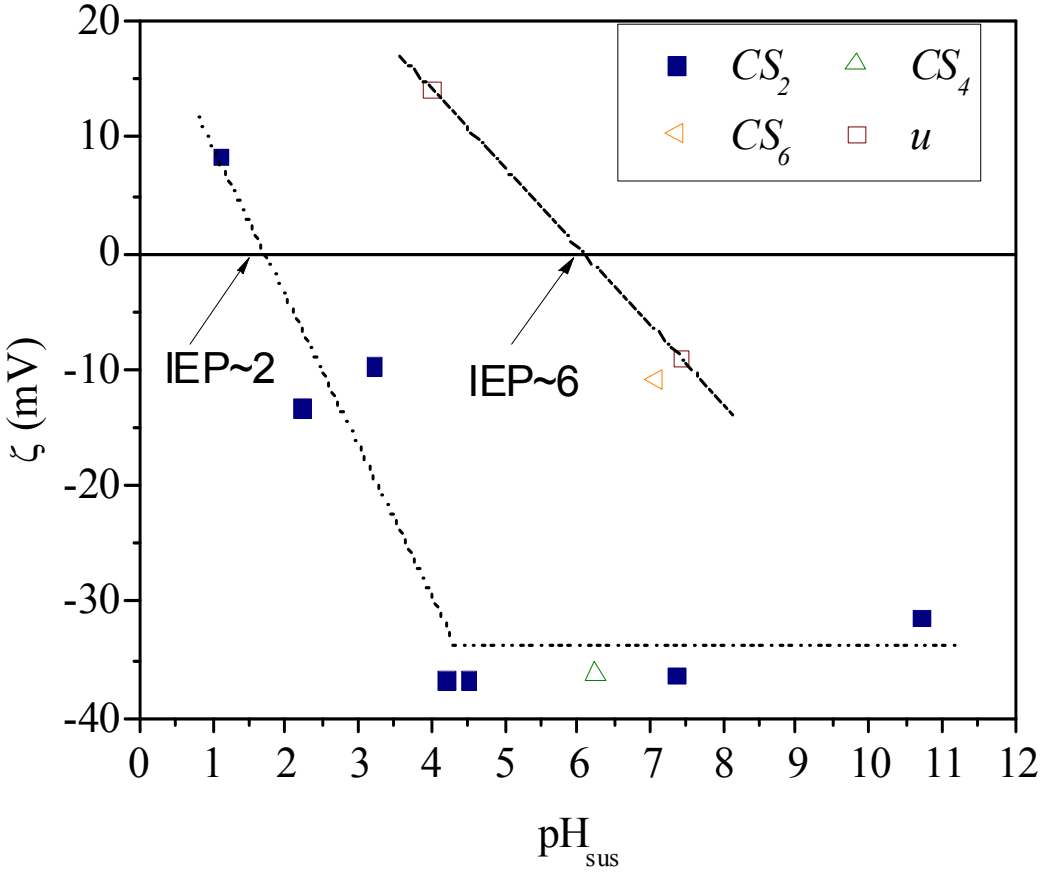

Figure 4: Mean Zeta potential (ζ) against suspension pH_{sus}. Lines stand to guide the eye and IEP for isoelectric point.

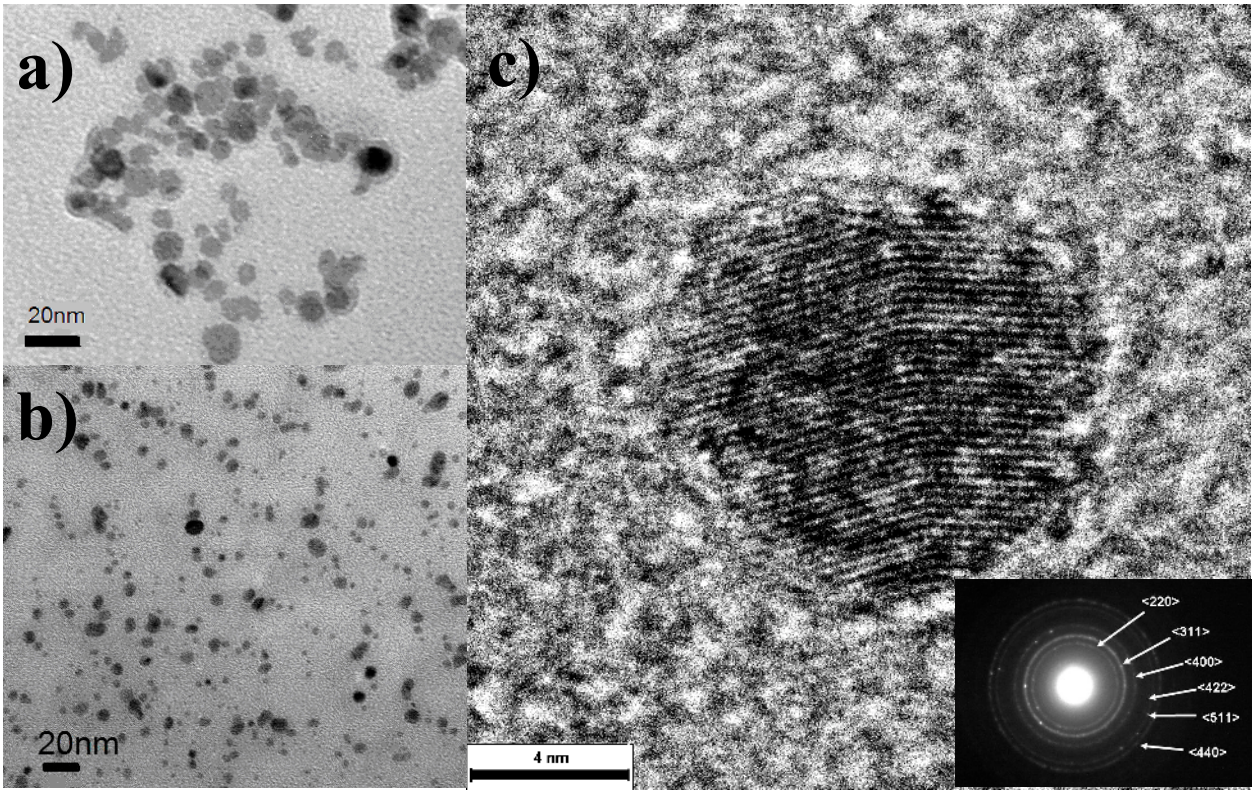

Figure 5: TEM images of uncoated (a) and citric acid coated particles (CS_6) (b), isolated particle of CS_6 dried colloid (c).

77

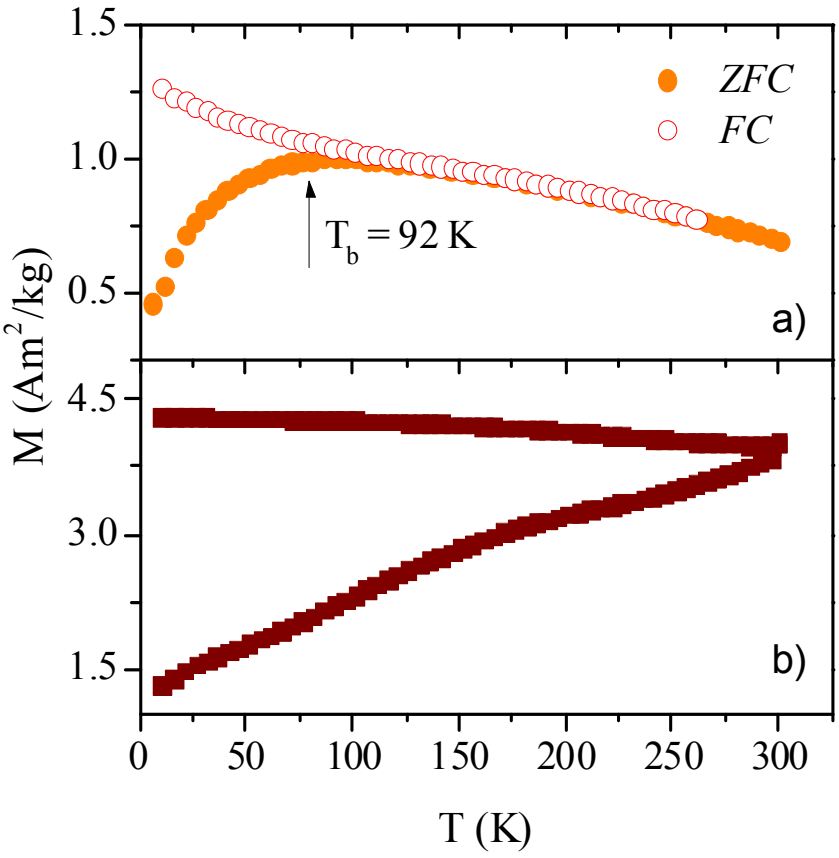

Figure 6: Specific magnetization temperature dependence for zero-field-cooled (ZFC) and field cooled (FC) protocols for: a) CS_2 and b) uncoated colloids (dried samples), acquired with H_{FC}=100 Oe and heating rates of 2 k/min

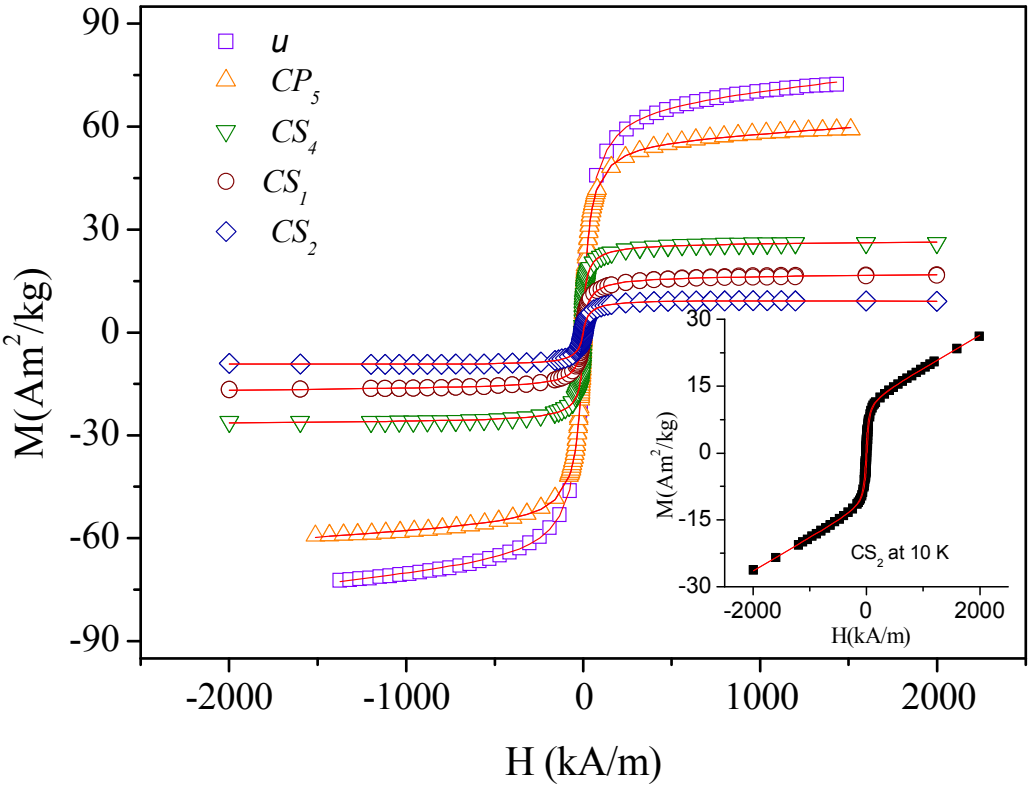

Figure 7: Specific magnetization loops measured at 290 K for various colloids. Inset: CS_2 measurement at 10 K. Solid lines stand for best Langevin fits using formula 2.

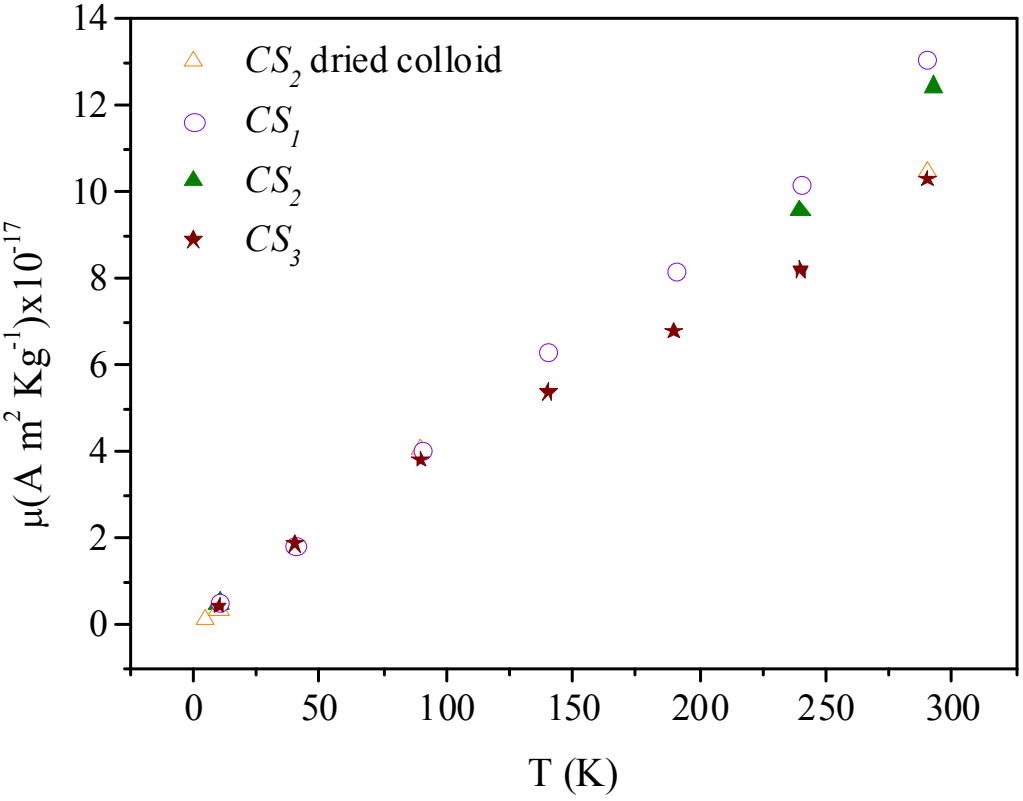

Figure 8: Mean magnetic moment derived from best fits of specific magnetization vs. applied field using formula 2, for various frozen colloids, colloids (290 K) and CS_2 dried powder.

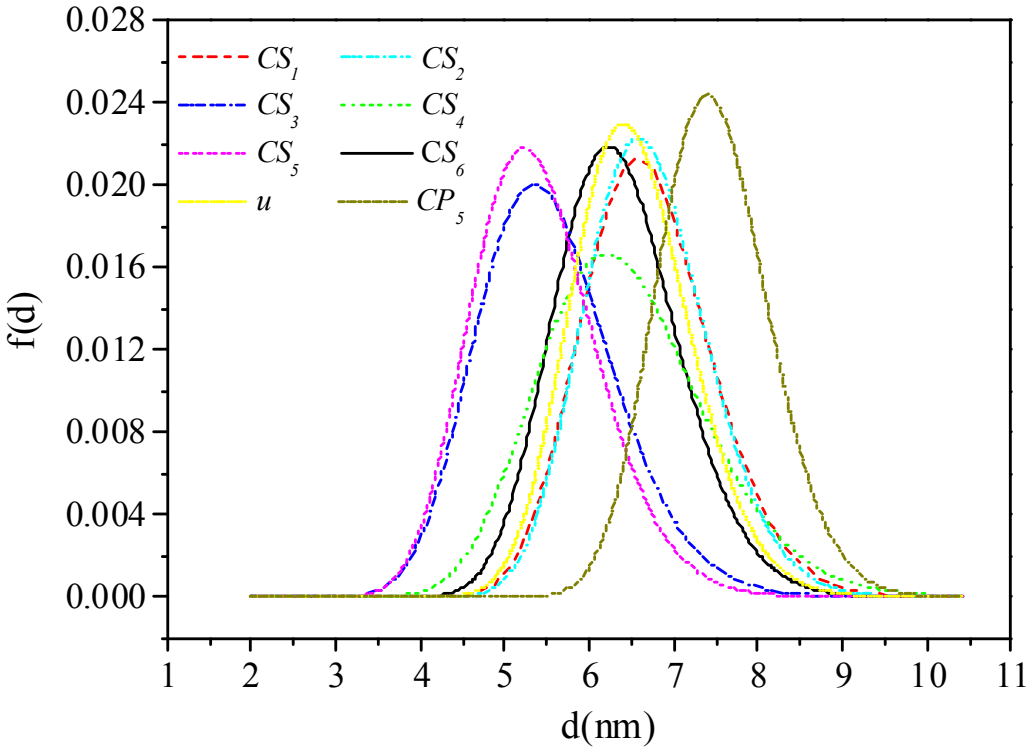

Figure 9: Log norm distribution of magnetic core diameters retrieved from the log norm magnetic moment distribution that fits the data in figure 7.

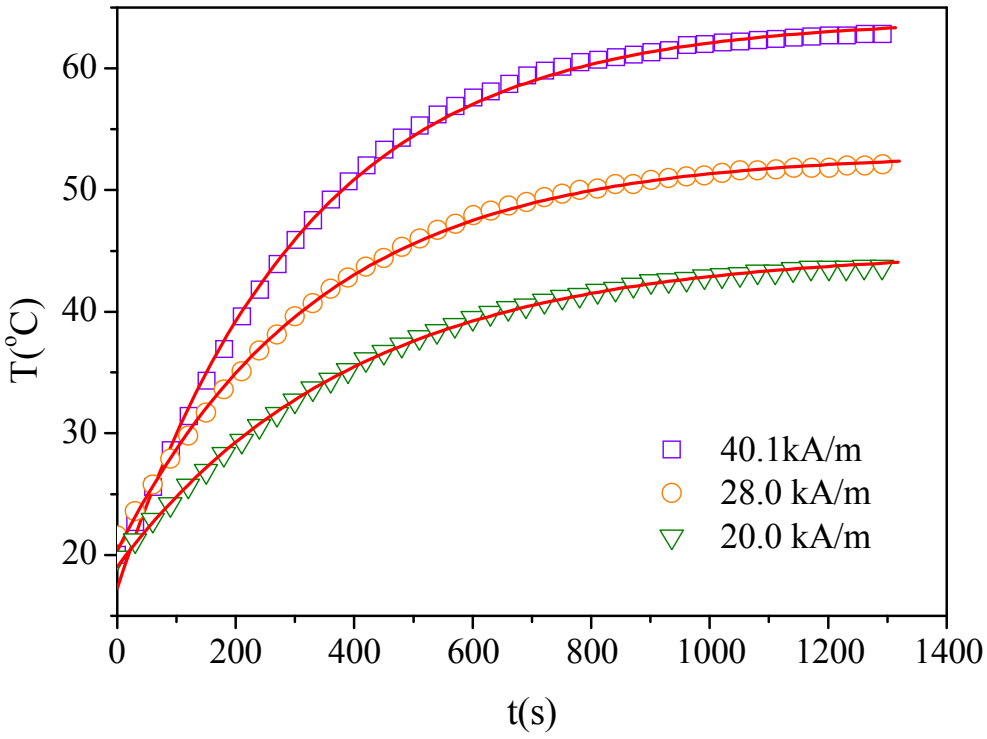

Figure 10: Heating curves at 265 kHz at various field amplitudes H_0.

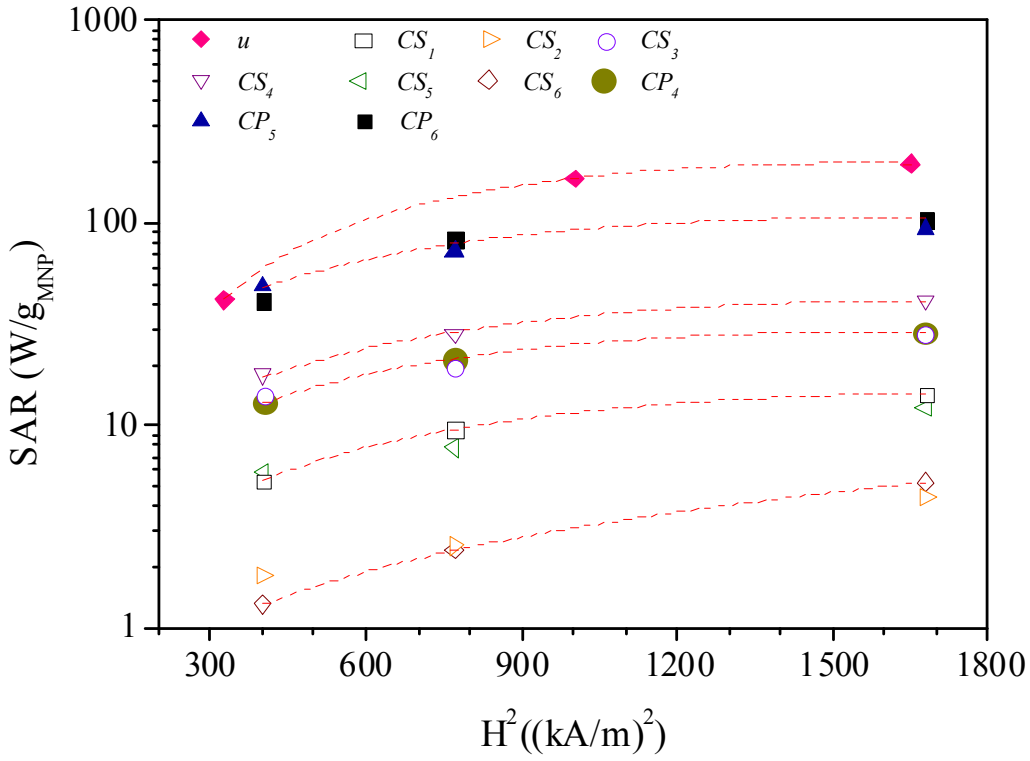

Figure 11: Specific absorption rate (SAR) field amplitude dependence. Doted lines stand for second order polynomial fits.

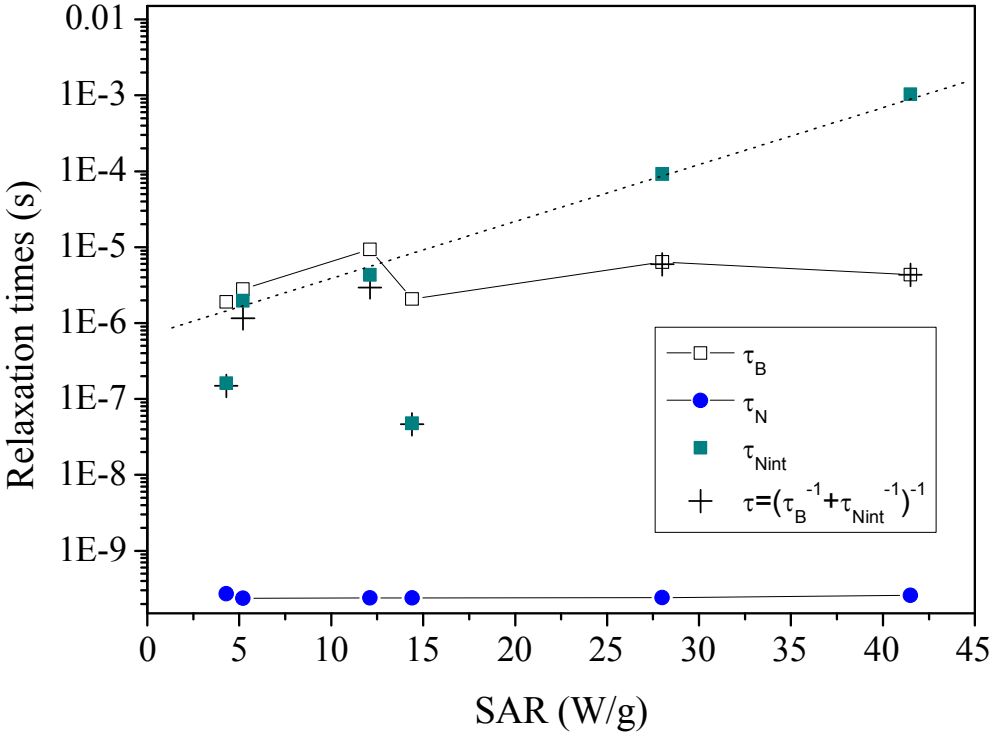

Figure 12: Brown relaxation times $\tau_B = \frac{3\eta V_H}{k_B T}$ calculated with $k_B = 1.3810^{-23}$ J K^{-1}, viscosity η=8.90 10^{-4} Pa s , T=300 K. Néel relaxation times $\tau_N = \tau_0 \exp(k_{eff} V / kT)$ of isolated nanoparticles calculated using size dependent anisotropy energy density $k_{eff}(d)$ and $\tau_0(d)$ interpolated from data in ref 31 and 32. Relaxation times τ_{Nint} for Néel mechanism taking into account size dependence and interaction.

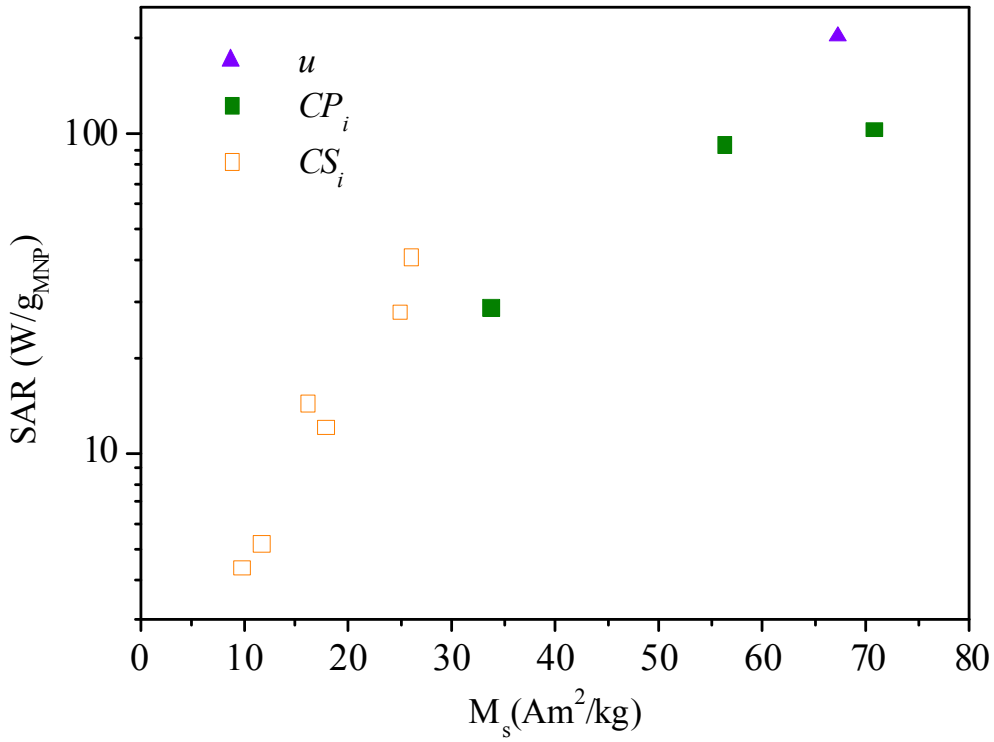

Figure 13: SAR dependence with specific saturation magnetization.

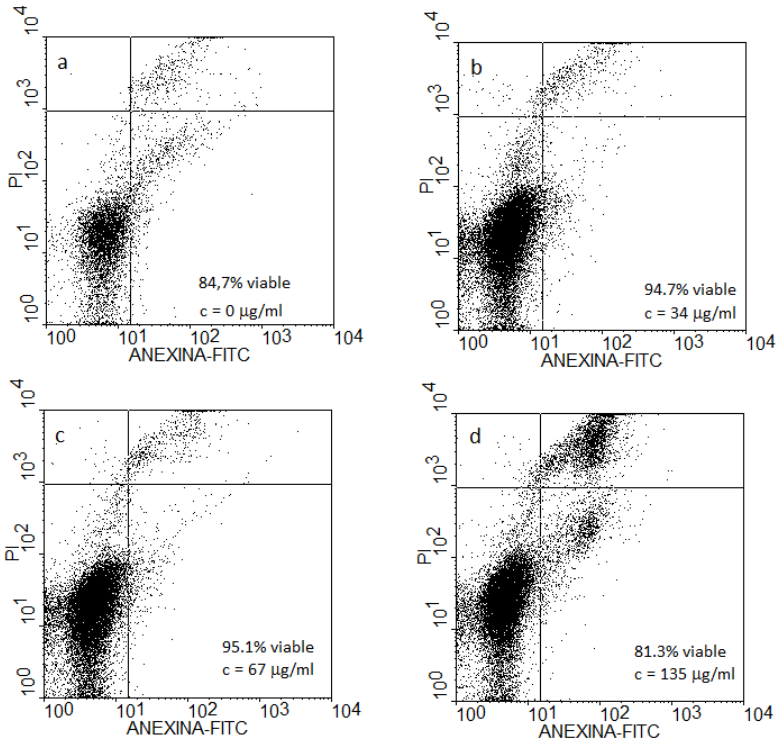

Figure 14: Dot plot obtained from FLOW CYTOMETRY data (Annexin/PI staining) of A549 cells. For all plots, Down Left (DL), Down Right (DR) and Up Right (UR) quadrants correspond to viable, apoptotic and necrotic cells respectively. Control (a), after 12 h internalization at 34 µg/ml (b), at 67 µg/ml (c), and 135 µg/ml (d).

TABLES

	[X] (g/l)	pH_{ads} ±0.01	pH_{sus} ±0.01	M_s (Am^2/kg)	d_m (nm)	σ_{dm}	δ (nm)	d_{TEM} (nm)	d_H (nm)	T_{Bi} (K)	T_B (K)	SAR (W/g)
CS_1	13.4	4.58	7.44	16.0	7.1	2.5	5.3	9.5±1.6	18.3	81	28	14.4
CS_2	10.7	4.91	7.34	9.7	7.0	2.4	7.5	8.2±2.4	17.8	92	41	4.29
CS_3	18.3	5.50	6.97	24.9	6.0	2.8	3.1	9.3±1.7	26.6	166	13	28.0
CS_4	13.1	6.25	7.22	26.0	7.1	3.4	3.4	11.9±3.5	23.4	196	18	41.5
CS_5	5.6	6.88	7.10	17.7	5.8	2.5	4.0	9.4±2.0	30.2	132	16	12.1
CS_6	7.4	7.08	7.22	11.5	6.7	2.4	6.4	10.9±1.8	20.2	126	32	5.2

Table I: Synthesis, magnetic and structural characterization parameters and specific absorption rate (SAR) under a radiofrequency field of 265 kHz and 40.1 kA/m of magnetite aqueous colloids, stable in suspension under moderate magnetic fields.

CS_i (i=1 to 6) labels colloids synthesized by one step co-precipitation at 60 °C, followed by citric acid adsorption at pH_{ads} medium acidity and finally suspended at pH_{susp}. [X] stands for concentration as mass of magnetite per solution volume; typical error is ± 0.2. Data derived from SQUID-DC magnetometry: M_s stands for specific saturation magnetization, d_m for magnetic core diameter, σ_{dm} for standard deviation and δ for twice the magnetically frustrated layer thickness. d_{TEM} stands for nanoparticle diameter retrieved from TEM images, d_H for weight – averaged nanoparticle hydrodynamic diameter, T_{Bi} for blocking temperatures determined from ZFC curve maximum, T_B blocking temperature for same size non interacting nanoparticles and SAR for Specific Absorption Rate at 40.1 kA/m and 265 kHz in Watts per gram of magnetite.

Colloid	u	CP_4	CP_5	CP_6
SAR(W/g)	203	28.78	93.6	104.2
M_s (Am^2/kg)	67.1	33.6	56.1	70.6
d_m (nm)	6.8	7.9	7.7	8.4
δ (nm)	0.6	3.2	1.2	0.6
[X]	8.28	6.1	10.2	6.0

Table II: Magnetic characterization and radiofrequency dissipation of magnetite stable aqueous colloids and uncoated colloid.

CP_i (i = 4, 5 and 6) labels colloids synthesized as detailed in table I and magnetically separated and u labels uncoated colloid. SAR stands for Specific Absorption Rate at 40.1 kA/m and 265 kHz in Watts per gram of magnetite. Data derived from SQUID-DC magnetometry: M_s stands for specific saturation magnetization, d_m for magnetic core diameter and δ for twice the magnetically frustrated layer thickness.

AUTHOR INFORMATION

Corresponding Author

* Marcela B. Fernández van Raap. raap@fisica.unlp.edu.ar

ACKNOWLEDGMENT

This work has been funded by CONICET (PIP 01111), ANPCyT (PICT 00898) and UNLP-X11/556 of Argentina. Z-potential measurements were performed at INQUISUR, UNS-CONICET by V. Lassalle whose help is deeply acknowledged. DC magnetrometry was performed using SQUID equipment of Red de Magnetismo y Materiales Magnéticos (RN3M) and VSM equipment of IFLP-CONICET. We thank FAPESP and C2NANO - Center for Nanocience and Nanotechnology/MCT (# 13872) for the used of TEM equipment. We greatly appreciate the help from R. Dewey and A. Correa of IIB-INTECH (UNSAM) with the flow cytometry analysis, and Y. Sosa and R. Goya for help with cell culture experiments, carried out at INIBIOLP – Patología B - CONICET. Marcela B. Fernández van Raap, Patricia Rivas, Pedro Mendoza Zélis, Gustavo Pasquevich and Francisco H. Sánchez are members of IFLP-CONICET, José L. Alessandrini member of Departamento de Física de la UNLP and M. Elisa de Sousa and Pablo Girardin are fellows of FONCYT and CONICET, Argentina.

ABBREVIATIONS

AS; ammonia solution; CA; citric acid; CP_i, i-th pellet colloid; CS_i, i-th supernatant colloid; DTA Differential thermal analysis; DLS, dynamic light scattering; d_H, hydrodynamic diameter;

DMEM, dulbeeco's modified eagle medium; FC, field cooling; IEP, isoelectric point; ISP, interacting superparamagnet; MNP, magnetic nanoparticles; PI, propidium iodide; pKa; acid dissociation constant; *u*-MNP, uncoated magnetic nanoparticles; *rf,* radiofrecuency; SAR, specific absorption rate; TEM, transmission electron microscopy; TG, thermogravimetry; XRD, x-ray diffraction; ZFC, zero field cooling; σ_{PI}; polydispersity index.

REFERENCES

(1) Rosensweig, R.; *Ferrohydrodynamics*, Dover books on physics, Dover Publications, **1997**

(2) Weinstein, J.S.; Varallyay, C. G.; Dosa, E.; Gahramanov, S.; Hamilton, B.; Rooney, W. D.; Muldoon L. L.; Neuwelt, E. A. *J Cereb Blood Flow Metab*. **2010**, 30 (1), 15–35.

(3) Gupta, A.K.; Gupta, M. *Biomaterials* **2005,** 26, 3995-4021.

(4) Smirnov, P. *Methods in Molecular Biology* **2009**, 512 (II), 333-353.

(5) Dobson, J. *Gene Therapy* **2006,** 13, 283–287.

(6) Chomoucka, J.; Drbohlavova, J.; Huska, D.; Adamb, V.; Kizek, R.; Hubalek, J. *Pharmacological Research* **2010,** 62, 144-149.

(7) Hilger, I.; Andrä, W.; Hergt, R.; Hiergeist, R.;Schubert, H.;Kaiser,W.A. *Radiology* **2001**, 218, 570–575.

(8) Silva, A.C.; Oliveira, T.R.; Mamani, J.B.; Malheiros, S.M.F.; Malavolta, L.; Pavon, L.F.; Sibov, T.T.; Amaro Jr, E.; Tannús, A.;Vidoto, E.L.G.; et al. *International Journal of Nanomedicine* **2011**, 6, 591-603.

(9) Gazeau, F.; Wilhelm, C. *Future Medicinal Chemistry* **2010**, 2 (3) , 397-408.

(10) Batlle, X.; Pérez, N.; Guardia, P.; Iglesias, O.; Labarta, A.; Bartolomé, F.; García, L.M.; Bartolomé, J.; Roca, A.G.; Morales, M.P.; et al. *J. Appl. Phys*. **2011**, 109, 1-6.

(11) Wei,W.; Quanguo, H.; Changzhong, J. *Nanoscale Res. Lett*. **2008**, 3, 397–415.

(12) Viota, J.L.; Arroyo, F.J.; Delgado, A.V.; Horno, J. *J. Colloid Interface Sci.* **2010**, 344 (1) , 144-149.

(13) Kogan, M. J.; Olmedo, M.J.I.; Hosta, L.; Guerrero, A.R.; Cruz, L.J.; Albericio, F. *Nanomedicine* **2007**, 2(3), 287-306.

(14) Campelj, S.; Makovec, D.; Drofenik, M. *J. Phys. Condens. Matter* **2008,** 20, 204101/1 - 204101/5.

(15) Rãcuciu, M. *Current Applied Physics* **2009**, 9(5), 1062-1066

(16) Nigama, S.; Barick, K.C.; Bahadur, D. *J. Mag. Magn. Mater.* **2011**, 323, 237-243

(17) Yallapua, M. M.; Othmanb, S. F.; Curtisb, E. T.; Guptaa, B. K.; Jaggia, M.; Chauhana, S. C. *Biomaterials* **2011**, 32, 1890–1905.

(18) Sahoo, Y.; Goodarzi, A.; Swihart, M. T.; Ohulchansky, T. Y.; Kaur N.; Furlani, E. P.; Prasad, P. N. *J. Phys. Chem. B* **2005**, 109, 3879-3885

(19) Rosensweig, R. E. *J. Magn. Magn. Mater.* **2002,** 252, 370-374.

(20) Massart, R. *IEEE Transactions on Magnetics* **1981**, MAG-17,(2), 1247–1248

(21) Lefebure, S.; Dubois, E.; Cabuil, V.; Neveu, S.; Massart, R. *J. Mater. Res.* **1998**, 13(10), 2975-2981.

(22) Sun, Z.; Su, F.; Forsling, W.; Samskog, P. *J. Colloids and Interface Science* **1998**, 197(1), 151–159.

(23) Provencher, S.W. *Comput. Phys. Commun.* **1982**, 27, 213-227.

(24) van Engeland, M.; Nieland, L. J. W.; Ramaekers, F. C.S.; Schutte, B.; Reutelingsperger, C.P.M. *Cytometry* **1998**, 31, 1-9.

(25) Shen, L.; Laibinis, P. E.; Hatton, T. A. *Langmuir* **1999**, 15, 447-453.

(26) Panias, D.; Taxiarchou, M.; Paspaliaris, I.; Kontopoulos, A. *Hydrometallurgy* **1996**, 42, 2, 257–265.

(27) Dutta, P.; Manivannan, A.; Seehra, M. S. *Phys. Rev. B* **2004**, 70, 174428, 1-7.

(28) Allia, P.; Coisson, M.; Tiberto, P.; Vinai, F.; Knobel, M.; Novak, M. A.; Nunes, W. C. *Phys. Rev. B* **2001**, 64(14), 1-12.

(29) Dormann, J. L.; Fiorani, D.; Tronc, E. *Magnetic Relaxation in Fine-Particle Systems,* Advances in Chemical Physics 98, Willey, **2007.**

(30) Raikher, Y. L.; Shliomis, M. I. *The effective field method in the orientational kinetics of magnetic fluids and liquid crystals*, Advances in Chemical Physics 87, Willey, Chapter 8. p595. **1994.**

(31) Gilmore, K.; Idzerda, Y.U.; Klem, M.T.; Allen, M.; T., Douglas; M., Young. *J. Appl. Phys.* **2005**, 97, 10B301/1-10B301/3.

(32) Fannin, P.C.; Marin, C.N.; Raj, K.; Couper, C.; Barvinschi, P. *J. Mag. Magn. Mater.* **2012**, 324, 3443-3447.

(33) Dormann, J.L.; Bessays, L.; Fiorani, D. *Solid State Phys. C* **1988**, 21, 2015-2034.

(34) Casals, E.; Gonzalez, E.; Puntes, V. F. *J. Phys. D: Appl. Phys.* **2012**, 45, 443001/1-443001/15.

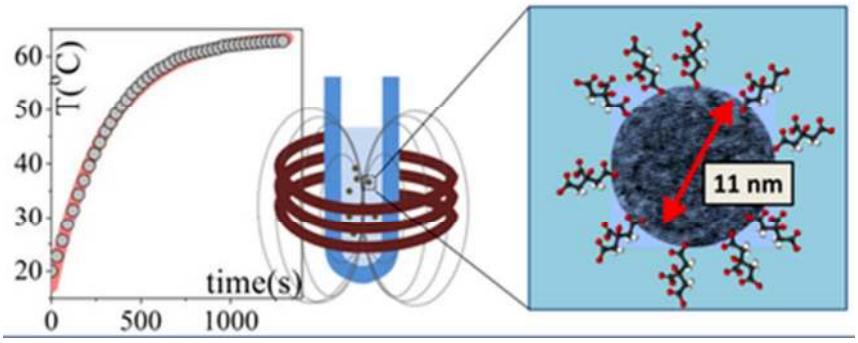

35x14mm (300 x 300 DPI)